

# Anticorrosive composite self-healing coating enabled by solar irradiation

Zhentao Hao<sup>1,2,3</sup>, Si Chen<sup>1,2,3</sup>, Zhifeng Lin (✉)<sup>1,2</sup>, Weihua Li (✉)<sup>1,2</sup>

<sup>1</sup> School of Chemical Engineering and Technology, Sun Yat-sen University, Zhuhai 519082, China

<sup>2</sup> Southern Marine Science and Engineering Guangdong Laboratory (Zhuhai), Sun Yat-sen University, Zhuhai 519082, China

<sup>3</sup> School of Materials Science and Engineering, Sun Yat-sen University, Guangzhou 510275, China

© Higher Education Press 2022

**Abstract** Self-healing coatings for long-term corrosion protection have received much interest in recent years. However, most self-healing coatings rely on healants released from microcapsules, dynamic bonds, shape memory, or thermoplastic materials, which generally suffer from limited healing times or harsh conditions for self-healing, such as high temperature and UV radiation. Herein, we present a composite coating with a self-healing function under easily accessible sunlight by adding Fe<sub>3</sub>O<sub>4</sub> nanoparticles and tetradecanol into epoxy resin. Tetradecanol, with its moderate melting point, and Fe<sub>3</sub>O<sub>4</sub> nanoparticles serve as a phase-change component and photothermal material in an epoxy coating system, respectively. Fe<sub>3</sub>O<sub>4</sub> nanoparticles endow this composite self-healing coating with good photothermal properties and a rapid thermal response time under simulated solar irradiation as well as outdoor real sunlight. Tetradecanol can flow to and fill defects by phase transition at low temperatures. Therefore, artificial defects created in this type of self-healing coating can be healed by the liquified tetradecanol induced by the photothermal effect of Fe<sub>3</sub>O<sub>4</sub> nanoparticles under simulated solar irradiation. The healed coating can still serve as a good barrier for the protection of the underlying carbon steel. These excellent properties make this self-healing coating an excellent candidate for various engineering applications.

**Keywords** self-healing coating, phase transition, photothermal effect, corrosion protection

## 1 Introduction

Organic coatings are widely used in marine engineering

Received August 24, 2021; accepted November 22, 2021

E-mails: linzhif6@mail.sysu.edu.cn (Lin Z.), liweihua3@mail.sysu.edu.cn (Li W.)

fields such as oil platforms, sea-crossing bridges, and shipments. However, as an effect of the harsh marine environment, microcracks and other defects are easily produced on the surface of organic coatings, resulting in penetration of water and other corrosive media and ultimately leading to coating failure. The use of self-healing coatings (SHCs) is a promising approach to realize long-term corrosion resistance because SHCs can heal microcracks and damage and form a healable physical barrier, which can significantly extend the life of coatings. To achieve a self-healing effect, one common approach involves adding healants or corrosion inhibitor-loaded microcapsules into polymeric resin [1–3]. When the coating is damaged, polymerizable healants or corrosion inhibitors inside microcapsules can be spontaneously released to the defect. These healants can form a dense film to fill the coating defect via polymerization, oxidation, coordination, or precipitation in response to metallic ions [4,5], pH [6–9], salt [10], oxygen [11–13], or UV radiation [11], providing a barrier against corrosive media. Another self-healing approach is based on dynamic bonds of polymer resin, such as hydrogen bonds [14–17] and disulfide bonds [18]. In this approach, broken resin chains in the damaged coating are reconnected by dynamic bonding interactions to reconstruct a physical barrier to protect the underlying metal. Such types of coatings can repair defects without adding external healants, showing excellent cyclic multirepairable performance. However, the two fractured surfaces in coating defects need to be manually laminated within the range of dynamic bonding action and require high temperature or UV irradiation for the construction of dynamic bond interactions. Other self-healing approaches include the use of thermoplastic resin or shape-memory materials. When the temperature exceeds the glass transition temperature ( $T_g$ ), the polymer resin can change from a glassy to a highly flexible state to repair defects. Likewise, shape-memory materials also exhibit a high

elastic state over a wide range of temperatures above the  $T_g$  or melting point and have a certain strength to facilitate the implementation of deformation. Unfortunately, achieving self-healing effect of these coatings also requires a high temperature to induce thermoplastic or shape memory properties [19]. Therefore, it is necessary to develop a new class of coatings with self-healing ability under relatively mild conditions.

Herein, we propose a sunlight-assisted SHC by incorporating commercially available  $\text{Fe}_3\text{O}_4$  nanoparticles and tetradecanol via a facile process.  $\text{Fe}_3\text{O}_4$  is a readily available magnetic photothermal conversion material with low cost and nontoxic properties. As a narrow bandgap semiconductor,  $\text{Fe}_3\text{O}_4$  has a wide range of light absorbance from the visible region to the near infrared region. Most solar photon energy is higher than the bandgap of  $\text{Fe}_3\text{O}_4$ , enabling the generation of above-bandgap electron-hole pairs. During relaxation of above-bandgap electron-hole pairs to the band edges, energy is converted into heat. Therefore,  $\text{Fe}_3\text{O}_4$  is considered a safe and universal photothermal material for photothermal therapies [20], solar steaming [21], and biosensors [22]. Tetradecanol is an environmentally friendly and readily accessible phase change material. It has a solid–solid phase transition and solid–liquid phase transition in the phase change process, allowing for a high thermal energy storage density [23,24] and enhanced thermal conductivity [25]. In the coating system, more importantly, tetradecanol is able to spontaneously flow and cover coating defects during the phase change process. Due to the combination of photothermal  $\text{Fe}_3\text{O}_4$  nanoparticles and the filling effects of tetradecanol, the coating reported herein demonstrates self-healing ability under solar irradiation. Both the intact and healed coating can protect the substrate from corrosion.

## 2 Experimental

### 2.1 Materials

Carbon steel (CS) plates were purchased from Hong Wang Co., Ltd. Before the experiment, CS plates were polished on 1000-grid sandpaper at a rotation speed of  $250 \text{ r}\cdot\text{min}^{-1}$  by a grinder polisher (VibroMet 2, Buehler Co., Ltd.). Then, the resultant CS plates were ultrasonically cleaned in acetone and deionized water. Commercial epoxy resin (E44) was purchased from Zhujiang Paint Co., Ltd. Ethanol, acetone, and NaCl are all analytical grade and were obtained from Sinopharm Chemical Reagent Co., Ltd.  $\text{Fe}_3\text{O}_4$  nanoparticles with an average particle size of 40 nm and tetradecanol were obtained from Shanghai Macklin Biochemical Co., Ltd. Deionized water was obtained from a Millipore purifi-

cation system. All reagents were used as received without any further purification.

### 2.2 Fabrication of a sunlight-assisted self-healing composite coating

The sunlight-induced SHC was prepared via a facile process. Specifically, different masses of tetradecanol (0.15, 0.5, 0.7, 1 g) as healing material were ultrasonically dissolved in ethanol (2 mL), followed by the addition of  $\text{Fe}_3\text{O}_4$  nanoparticles (0.1 g). The corresponding mass fractions of tetradecanol were 4.8, 14.5, 19.1, and 25.3 wt% in the composite coatings. Then, commercial epoxy resin (2 g) and amine curing agent (0.86 g) were added to the mixture at ambient temperature under vigorous mechanical stirring for 10 min with a rotation speed of  $1000 \text{ r}\cdot\text{min}^{-1}$ . The mixed dispersion was subsequently coated on a CS plate at a coating speed of  $50 \text{ mm}\cdot\text{s}^{-1}$  controlled by a mini automatic coating applicator (BEVS-1188, BEVS Industrial Co., Ltd.). Finally, after curing at room temperature for 48 h, a self-repairing coating was obtained. The thickness of the obtained coating was ca. 200  $\mu\text{m}$ .

### 2.3 Characterization

The morphology of the SHC samples was observed by scanning electron microscopy (SEM, JOEL 400F). The attenuated total reflection Fourier transform infrared spectroscopy (ATR-FITR) spectrum at the wavelength range of 4000–500 nm was measured by Fourier transform infrared spectrometry (EQUINOX 6000). UV-visible spectra were measured by a UV-vis spectrophotometer (UV-2501PC) in the wavelength range of 200–1400 nm. The surface temperature of samples under simulated solar irradiation was automatically recorded every 10 s by an infrared imager (Fluke Ti10). Differential scanning calorimetry (DSC) measurements were conducted on a differential scanning calorimeter (Perkin-Elmer DSC-7) under a  $40 \text{ mL}\cdot\text{min}^{-1}$  nitrogen flow. Samples were heated to 80  $^{\circ}\text{C}$  at a rate of  $10 \text{ }^{\circ}\text{C}\cdot\text{min}^{-1}$  and naturally cooled to room temperature.

### 2.4 Self-healing test

Samples with a tetradecanol mass fraction of 25.3 wt% were used for subsequent tests. In the self-healing test, the coating sample was damaged by a scalpel to form a pit or scratch. Then, the damaged sample was placed under a xenon lamp for 3 min to test the healing effect. A xenon lamp (PLSSXE300/300UV) equipped with a solar filter was used to provide simulated solar irradiation, which was located 18 cm above the sample. The morphology of the coatings before and after healing was observed by optical microscopy. The surface potential distribution of the sample was monitored by scanning Kelvin probe

(SKP, Ametek Inc.) in the atmosphere. During this test, SKP was located ca. 100  $\mu\text{m}$  above the sample with a scanning area of 3 mm  $\times$  4 mm.

## 2.5 Corrosion resistance test

Electrochemical impedance spectroscopy (EIS) was performed to evaluate the anti-corrosion performance of the coating. The test was conducted in a 3.5 wt% NaCl aqueous solution by an electrochemical workstation (Gamry 600). In the EIS test, coating samples serve as working electrodes with an exposed area of 1 cm<sup>2</sup>. Pt and saturated calomel electrodes were used as counter and reference electrodes, respectively. Then, EIS was conducted with an alternating voltage of 10 mV with frequencies ranging from 10<sup>5</sup> to 10<sup>-2</sup> Hz.

## 2.6 Wettability test

The wettability of the SHCs was evaluated by static contact angle, which was measured on an OCA20 instrument (Data Physics) by dispensing a 3  $\mu\text{L}$  water droplet on the coating using the sessile method at ambient temperature (25  $\pm$  2  $^{\circ}\text{C}$ ).

# 3 Results and discussion

## 3.1 Characterization of the SHC

The fabrication process and ATR-FTIR of the SHC is illustrated in Fig. 1. The tetradecanol and Fe<sub>3</sub>O<sub>4</sub> nanoparticles were uniformly dispersed in ethanol, followed by the addition of epoxy oligomer and amine curing agent. After adequate stirring, the mixture was rapidly coated on CS by a coating applicator and dried at room temperature for 48 h. A SHC was obtained after the evaporation of ethanol and adequate crosslinking of epoxy resin (Fig. 1(a)). The obtained samples were used for subsequent characterizations and tests.

The successful incorporation of the Fe<sub>3</sub>O<sub>4</sub> nanoparticles and tetradecanol into the epoxy resin were verified by the ATR-FTIR spectrum. Figure 1(b) shows that the peak identified at 3334 cm<sup>-1</sup> corresponds to the broad O–H stretching vibration in alcohol. Peaks at 2918 and 2848 cm<sup>-1</sup> are attributed to the stretching vibration of C–H for tetradecanol. The peak at 1062 cm<sup>-1</sup> is attributed to the vibration of C–O, while that at 1463 cm<sup>-1</sup> is associated with the –OH stretching vibration [26]. In the Fe<sub>3</sub>O<sub>4</sub> spectrum, the broad band at 581 cm<sup>-1</sup> corresponds to Fe–O stretching vibrations. In the case of the SHC, peaks are observed at 3334, 1062, 2918, and 2848 cm<sup>-1</sup>, which is consistent with tetradecanol. Peaks at 1062 and 1463 cm<sup>-1</sup> are also found in the SHC. In addition, a

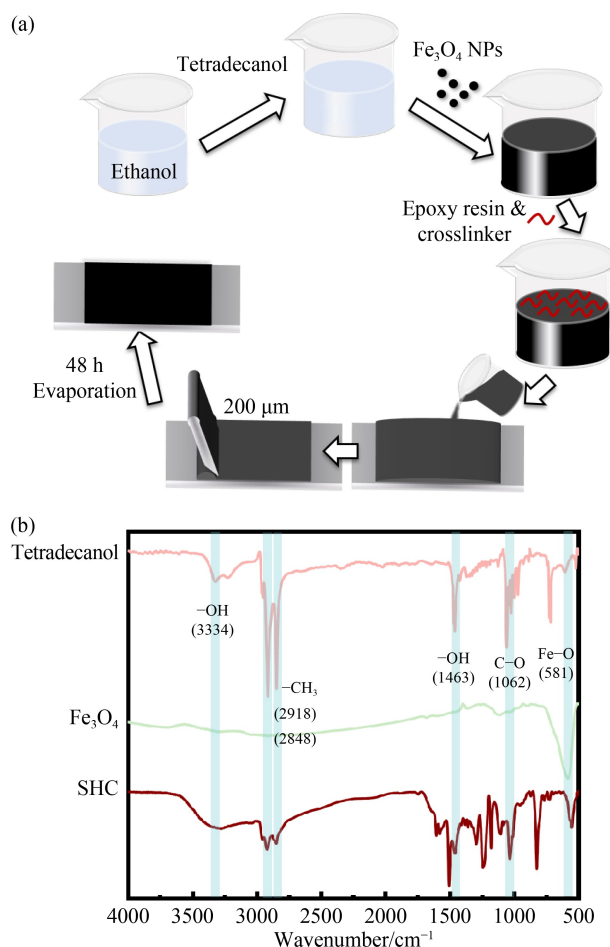


**Fig. 1** (a) Schematic illustration of the facile fabrication process of the composite SHC; (b) ATR-FTIR spectra of the tetradecanol, Fe<sub>3</sub>O<sub>4</sub> and the SHC.

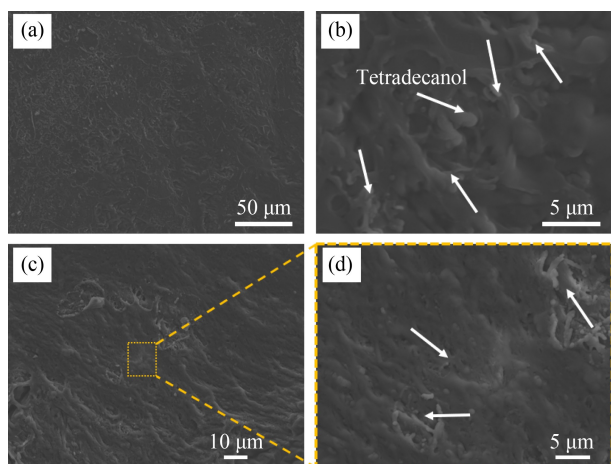
bathohypochromic shift is observed for characteristic peaks of Fe–O in the spectrum of the SHC compared to that of Fe<sub>3</sub>O<sub>4</sub>, which may stem from the doping of epoxy resin. This indicates that tetradecanol and Fe<sub>3</sub>O<sub>4</sub> were successfully integrated with the epoxy resin.

Figure 2 shows the morphology and cross-section of samples. The wax-like morphology of the SHC surface is due to the presence of tetradecanol (Figs. 2(a) and 2(b)). The cross-section of the SHC shows that tetradecanol accumulates inside the epoxy resin (Figs. 2(c) and 2(d)). As the mass fraction of tetradecanol increases, more tetradecanol precipitates on the surface of the epoxy resin (Fig. 3). The image also shows that the coating has a dense structure with no defects at the cross-section. The contact angle of water decreases as the content of tetradecanol increases. This may be due to the presence of more polar hydroxyl groups on the surface.

## 3.2 Photothermal-responsive performance of SHC

The photothermal performance of coatings is essential for inducing self-healing behavior. Therefore, we conducted





**Fig. 2** SEM of the SHC coating with magnifications of (a) 500 × and (b) 5000 ×; cross-sections of the SHC with magnifications of (c) 1000 × and (d) 3000 ×; white arrows refer to the position of tetradecanol.

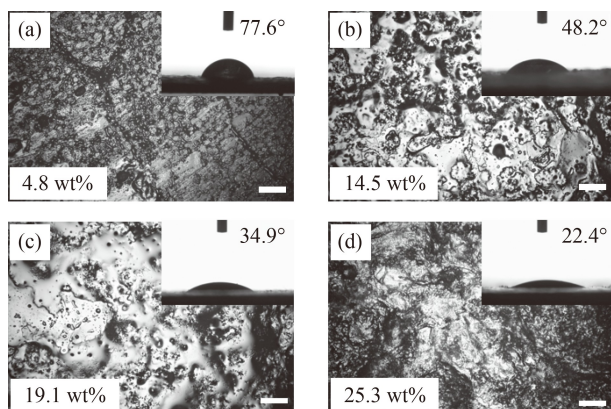


**Fig. 3** Optical images of the surface morphology and wettability evolution of SHCs with different mass fractions of tetradecanol: (a) 4.8 wt%, (b) 14.5 wt%, (c) 19.1 wt%, and (d) 25.3 wt%; bars in all images represent 150 μm.

a photothermal response test of the SHC with simulated solar irradiation and results are shown in Fig. 4. Figure 4(a) presents infrared images of the coating over time. It can be seen from Fig. 4(b) that after 200 s of irradiation, the temperature of the SHC increases and gradually reaches approximately 70 °C because of the photothermal effect of  $\text{Fe}_3\text{O}_4$  nanoparticles. In contrast, in the absence of  $\text{Fe}_3\text{O}_4$  nanoparticles, the temperature of the control sample only increases to approximately 35 °C, showing limited photothermal efficiency. UV-vis spectral results indicate that  $\text{Fe}_3\text{O}_4$  nanoparticles can absorb ultraviolet light with a wavelength of 200 to 1400 nm, which enables the effective absorption of sunlight (Fig. 4(c)). After  $\text{Fe}_3\text{O}_4$  nanoparticles are integrated with tetradecanol epoxy resin, the resulting SHC still has a wide light absorption range from infrared to ultraviolet. DSC analysis shows that pure tetradecanol shows one endothermic peak in the melting process but two exothermic peaks in the freezing process. This is attributed to the presence of a

metastable hexagonal orthorhombic solid phase ( $S_{\text{HEX}}$ ) and orthorhombic solid phase ( $S_{\text{ORT}}$ ) of solid fatty alcohol [27]. In the freezing process, the former exothermic peak is due to the transformation from the liquid form to  $S_{\text{HEX}}$ , while the latter exothermic peak is attributed to the transformation from  $S_{\text{HEX}}$  to  $S_{\text{ORT}}$ . Nevertheless, in the melting process, the two phase transition processes are very close, showing only one visible endothermic peak. The DSC curve of the SHC is very similar to that of tetradecanol. Compared with pure tetradecanol, there is a decrease in intensity and area in both the endothermic and exothermic peaks due to the presence of epoxy resin. In addition, the melting temperature ( $T_m$ ) and freezing temperature ( $T_f$ ) of pure tetradecanol can also be determined from DSC analysis. Tetradecanol starts to absorb heat at approximately 37.6 °C, which is also the melting point of tetradecanol. This indicates that tetradecanol starts to melt into a liquid. There is a symmetrical peak at 40.3 °C, showing that nonpolymeric tetradecanol has the fastest melting rate (Fig. 4(d)). In the freezing process, tetradecanol begins to release heat at a  $T_f$  of ca. 33.8 °C. The  $T_m$  and  $T_f$  of the SHC are similar to those of pure tetradecanol, which plays a major role in the phase transition. Additionally, the photothermal properties of the  $\text{Fe}_3\text{O}_4$  nanoparticles show no observable change after five simulated solar irradiation on-off heating cycles, as shown in Fig. 4(e).

### 3.3 Solar-driven self-healing property of the coatings

Self-healing is of great significance in this work. To verify the self-healing property of the prepared coatings, artificial defects, including perforations and scratches, were prepared by a scalpel, as shown in Fig. 5. After irradiation with a simulated solar lamp, the perforation is filled with tetradecanol (Fig. 5(a)). A similar result can also be observed from Fig. 5(b), in which the scratch is also fixed. The self-healing mechanism of the coating is illustrated in Fig. 5(c).  $\text{Fe}_3\text{O}_4$  is a metal oxide-based semiconductor with a narrow bandgap. Above-bandgap electron-hole pairs are formed under high-energy solar irradiation. The relaxation of these above-bandgap electron-hole pairs to the band edges allows conversion of the extra energy into heat [28]. Then, the heat is spontaneously transferred from high-temperature  $\text{Fe}_3\text{O}_4$  nanoparticles to adjacent tetradecanol via heat conduction without intermixing of any material [29], leading to the melting of tetradecanol. Then, liquefied tetradecanol flows and fills defects to achieve a self-healing effect.

Although the SHC can heal scratches under a simulated solar lamp, it is still unknown whether it is effective under real solar irradiation. To verify the performance of this coating in practical applications, we placed a scratched sample under outdoor sunlight. The entire self-healing process is demonstrated in Fig. 6. The surface potential distribution of the SHC was recorded by SKP.

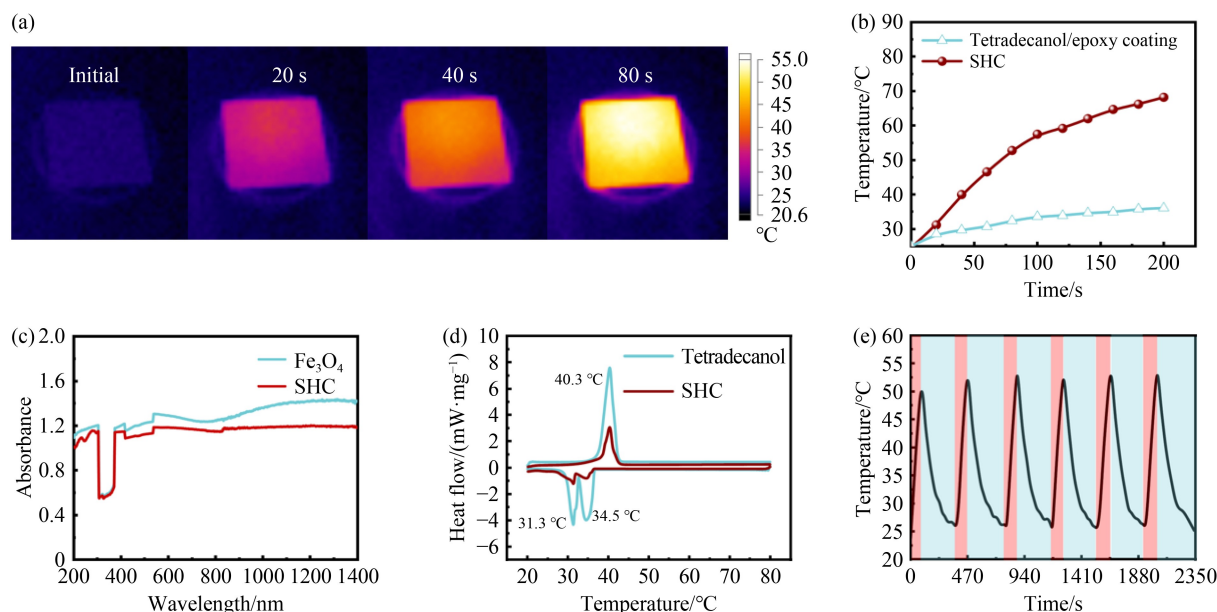


**Fig. 4** (a) Infrared thermal images and surface temperature evolution of the SHC with time under simulated solar irradiation; (b) surface temperature evolution of coatings under simulated solar irradiation with time; (c) UV-vis spectra of  $\text{Fe}_3\text{O}_4$  nanoparticles and the SHC; (d) DSC curves of tetradecanol and the SHC in the 20–80 °C temperature range; (e) cyclic photothermal responsive performance of the SHC.

Under irradiation with sunlight, the scratch was observed to gradually disappear with time during the irradiation process, suggesting that sunlight can serve as an effective stimulus to induce the self-healing process (Fig. 6(a)). In the initial stage, the surface potential distribution of the defect has an average potential of  $-1600$  mV, which is higher than that of other intact regions with a potential of  $-3200$  mV (Fig. 6(b)). Accordingly, the SKP potential of the healed surface becomes relatively uniform after the scratch is healed (Fig. 6(c)). Under solar irradiation, the healing behavior of the SHC is completely autonomous by the phase transition of tetradecanol without other interventions, such as pH, moisture, or other healing materials, which is of considerable technical and commercial importance. The role of tetradecanol is vital for realization of the self-healing effect. Pure epoxy,  $\text{Fe}_3\text{O}_4$ /epoxy, and tetradecanol/epoxy coatings fail to show self-healing properties under solar irradiation for 30 min as shown in Fig. S1 (cf. Electronic Supplementary Material, ESM). The  $\text{Fe}_3\text{O}_4$ /epoxy coating without tetradecanol fails to heal the scratch compared with the  $\text{Fe}_3\text{O}_4$ /tetradecanol/epoxy coating, because there is no liquefied phase change material to fill the defect. In the case of the tetradecanol/epoxy coating, there are no photothermal particles present to heat the phase change material, also resulting in a lack of self-healing ability. Coatings with a low content of tetradecanol fail to adequately cover the defect and cannot form a good barrier against corrosive media.

### 3.4 Corrosion resistance performance of coatings

Protective performance is one of the most important

properties of anticorrosive coatings. In this study, EIS was conducted to evaluate the protective properties of coatings on a metal substrate in 3.5 wt% NaCl. Figure 7 presents EIS plots of CS and epoxy-coated CS, in which the overall anti-corrosion performance can be reflected by the modulus impedance at low frequency ( $|Z|_{0.01\text{Hz}}$ ) due to the high relevance with charge transfer processes at the CS/barrier layer interface. Higher values of  $|Z|$  indicate a lower corrosion rate [30–32]. Without the protection of the coating,  $|Z|_{0.01\text{Hz}}$  of the bare CS is ca.  $10^3 \Omega\cdot\text{cm}^2$ . In contrast, in the presence of the SHC,  $|Z|_{0.01\text{Hz}}$  increases to ca.  $10^7 \Omega\cdot\text{cm}^2$ , nearly four orders of magnitude higher than CS (Figs. 7(a) and 7(b)). The  $|Z|_{0.01\text{Hz}}$  of the SHC is on the same order of magnitude as that of commercial pure epoxy resin (Fig. S2, cf. ESM). In the Bode-phase plot, the time constant at high frequency and low frequency represents capacitance of coatings and corrosion response of the CS, respectively. For the bare CS, there is only one time constant in the Bode-phase plot, suggesting that the corrosive media are in direct contact with CS and corrosion reactions occur. For the SHC-coated sample, there are two time constants, but it shows one broad peak because the epoxy coating can serve as a good barrier to prevent penetration of  $\text{O}_2$ ,  $\text{H}_2\text{O}$ , and  $\text{Cl}^-$ . To understand the corrosion process of these two cases, equivalent circuit models were used to fit these EIS plots, as shown in Figs. 7(c) and 7(d). Due to the intactness and insulation of the coating, in this electrochemical system, when alternating voltages are applied, electrolyte/coating and coating/CS interfaces can be regarded as two series-connected capacitors. Therefore,  $R(\text{QR})(\text{QR})$  was selected to fit the EIS plot of epoxy-coated CS. The fitted electro-

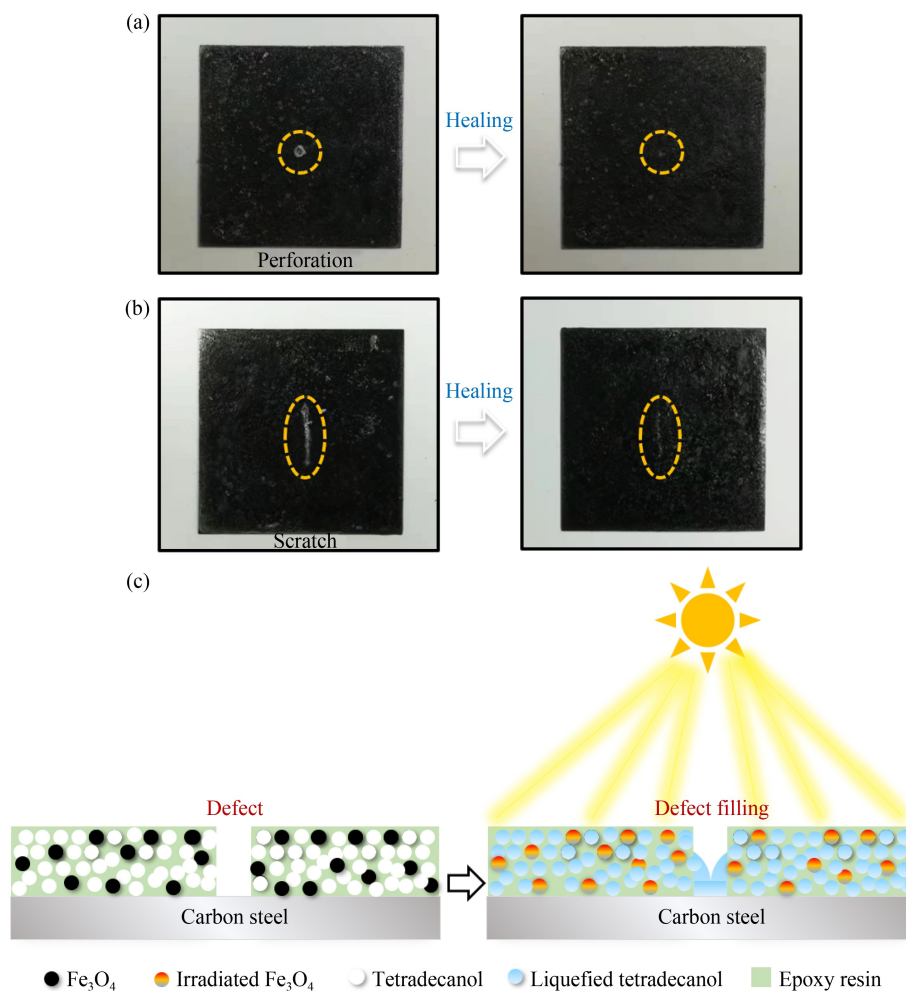


**Fig. 5** Images of SHCs with different types of damage: (a) perforation and (b) scratch before and after healing; (c) schematic illustration of the self-healing mechanism of the SHC.

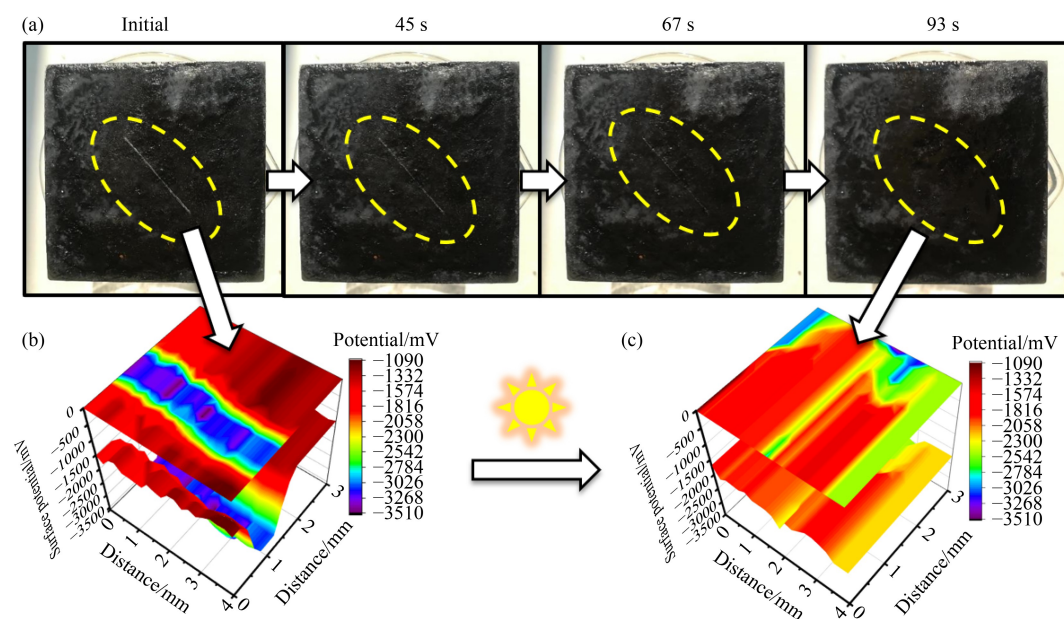


**Fig. 6** (a) The self-healing process of the SHC under outdoor irradiation with sunlight; surface potential distribution of (b) the damaged SHC and (c) healed SHC recorded by SKP.



chemical parameters are provided in Table 1.  $R_s$ ,  $R_f$  and  $R_{ct}$  refer to the resistance of the NaCl aqueous solution, coating, and charge-transfer resistance, respectively.  $Q_f$  and  $Q_{dl}$  represent constant phase elements (CPEs) modeling the capacitance of the coating/electrolyte interface and the electrical double layer capacitance at the coating layer/CS interface, respectively. The impedance of the CPE can be expressed as [33,34]:

$$Z_{CPE} = Y_0^{-1}(j\omega)^{-n}, \quad (1)$$

where  $Y_0$ ,  $j$ , and  $\omega$  refer to the CPE coefficient, imaginary unit, and angular frequency, respectively, and  $n$  is the exponent reflecting deviations from ideal capacitance due

to roughness or surface defects. The  $R_{ct}$  of epoxy resin-coated CS is three magnitudes higher than that of bare CS. The corrosion protection efficiency ( $\eta$ ) can be calculated by:

$$\eta = \frac{R_{ct} - R'_{ct}}{R_{ct}} \times 100\%, \quad (2)$$

where  $R'_{ct}$  and  $R_{ct}$  refer to the charge transfer resistance of the CS before and after being coated by the SHC, respectively. The as-calculated protection efficiency can reach up to 99.83%. In addition, the  $Q_f$  of the SHC is close to that of commercial pure epoxy resin (Table 1), suggesting that the SHC has low permeability comparable

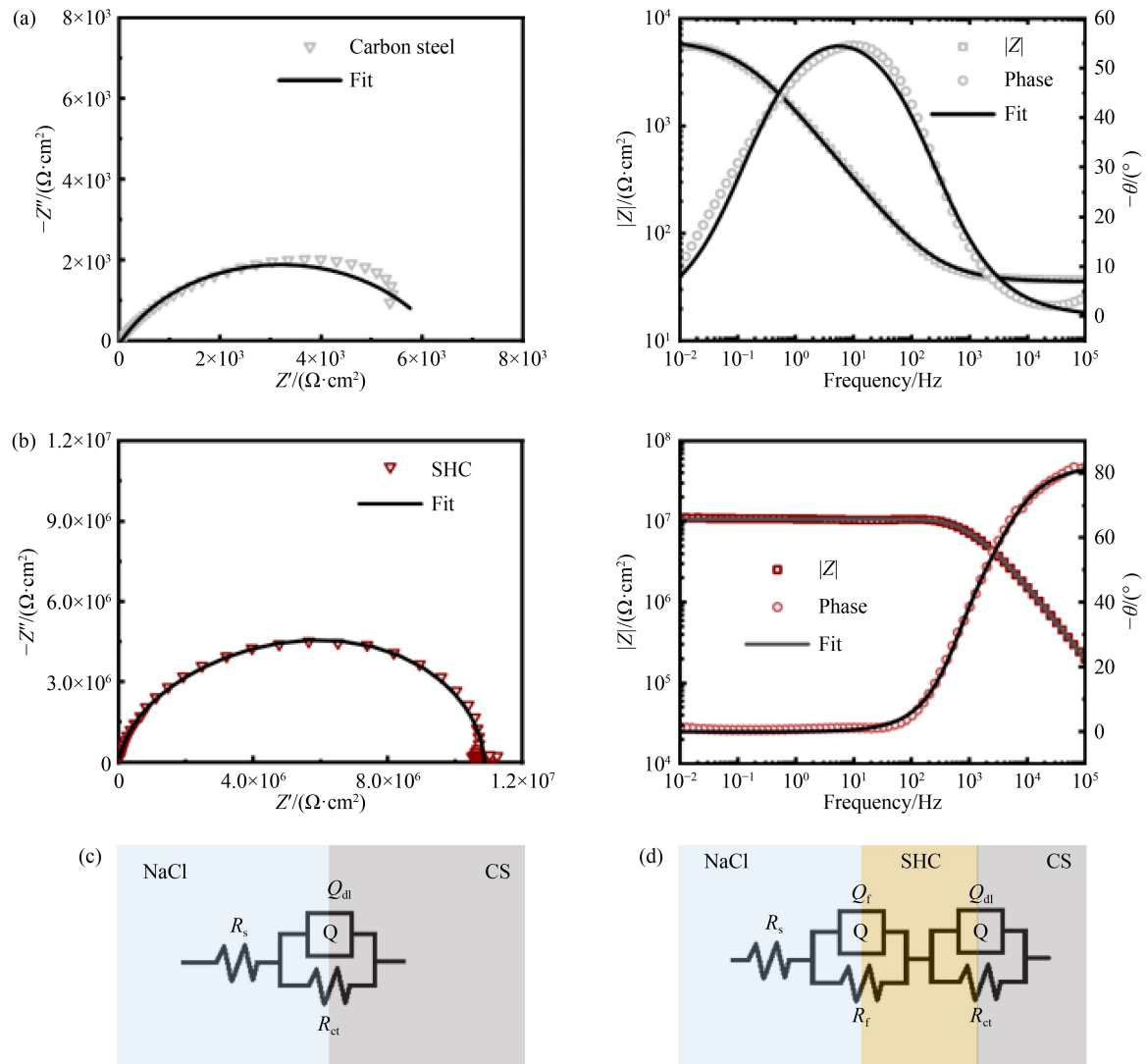


Fig. 7 Nyquist and Bode plots of the (a) bare CS and (b) SHC-coated CS; equivalent circuits of the (c) bare CS and (d) SHC-coated CS.

Table 1 Electrochemical parameters of bare CS, epoxy resin-coated CS, and the intact SHC-coated CS

Material	$R_f/(\Omega \cdot \text{cm}^2)$	$Q_f - Y_0/(\text{F} \cdot \text{cm}^{-2} \cdot \text{s}^{n-1})$	$Q_f - n$	$R_{ct}/(\Omega \cdot \text{cm}^2)$	$Q_{dl} - Y_0/(\text{F} \cdot \text{cm}^{-2} \cdot \text{s}^{n-1})$	$Q_{dl} - n$
CS	—	—	—	$6.33 \times 10^3$	$1.84 \times 10^{-4}$	0.69
Epoxy resin-coated CS	$2.16 \times 10^7$	$4.86 \times 10^{-11}$	0.95	$1.19 \times 10^7$	$3.36 \times 10^{-10}$	0.93
SHC-coated CS	$7.02 \times 10^6$	$3.28 \times 10^{-11}$	0.98	$3.84 \times 10^6$	$4.70 \times 10^{-11}$	0.89

to a commercial coating. Additionally,  $Q_{dl}$  can serve as an indicator to describe the corrosion reaction site on the metal interface. A higher value of  $Q_{dl}$  indicates more corrosion reactions on metal sites. It is worth noting that the  $Q_{dl}$  of the SHC-coated CS decreases to ca.  $10^{-11} \text{ F}\cdot\text{cm}^{-2}\cdot\text{s}^{n-1}$ , much lower than that of bare CS, showing decreased corrosion active sites on the underlying CS.

### 3.5 Self-healing performance of coatings in corrosion protection

Figure 8 presents a comparison of the damaged coating before and after healed in corrosion resistance. Figures 8(a) and 8(b) show EIS plots of the damaged and healed coatings, respectively. A typical model for a defect-containing coating is shown in Fig. 8(c). Due to the penetration of conductive electrolyte through the coating defect, metal is directly exposed to electrolyte. In this electrochemical system, when an alternating voltage is

applied, capacitors occur at electrolyte/coating and electrolyte/CS interfaces, which are connected in parallel.  $Q_f$  and  $Q_{dl}$  refer to the capacitance at the electrolyte/coating layer and damaged area/CS interfaces, respectively. For the damaged SHC,  $|Z|_{0.01\text{Hz}}$  and  $R_{ct}$  decrease to ca.  $10^3 \Omega\cdot\text{cm}^2$ . This is on the same order of magnitude as bare CS because the corrosive solution directly contacts the CS surface at the defect region. In addition, the  $Q_f$  of the SHC increases after damage (Table 2), revealing a high coating permeability. Another piece of evidence is that there are two visible peaks in the Bode plot (Fig. 8(a)), which usually reflects that aggressive species have contacted the surface of the CS during immersion. However, after the aforementioned healing process under simulated solar irradiation (Fig. 9), both  $|Z|_{0.01\text{Hz}}$  and  $R_{ct}$  increase to ca.  $10^6 \Omega\cdot\text{cm}^2$ , which is only one order of magnitude lower than that of the original intact coating. The  $R_f$  of the healed SHC increases to ca.  $10^5 \Omega\cdot\text{cm}^2$ , suggesting enhanced resistance for corrosion media to

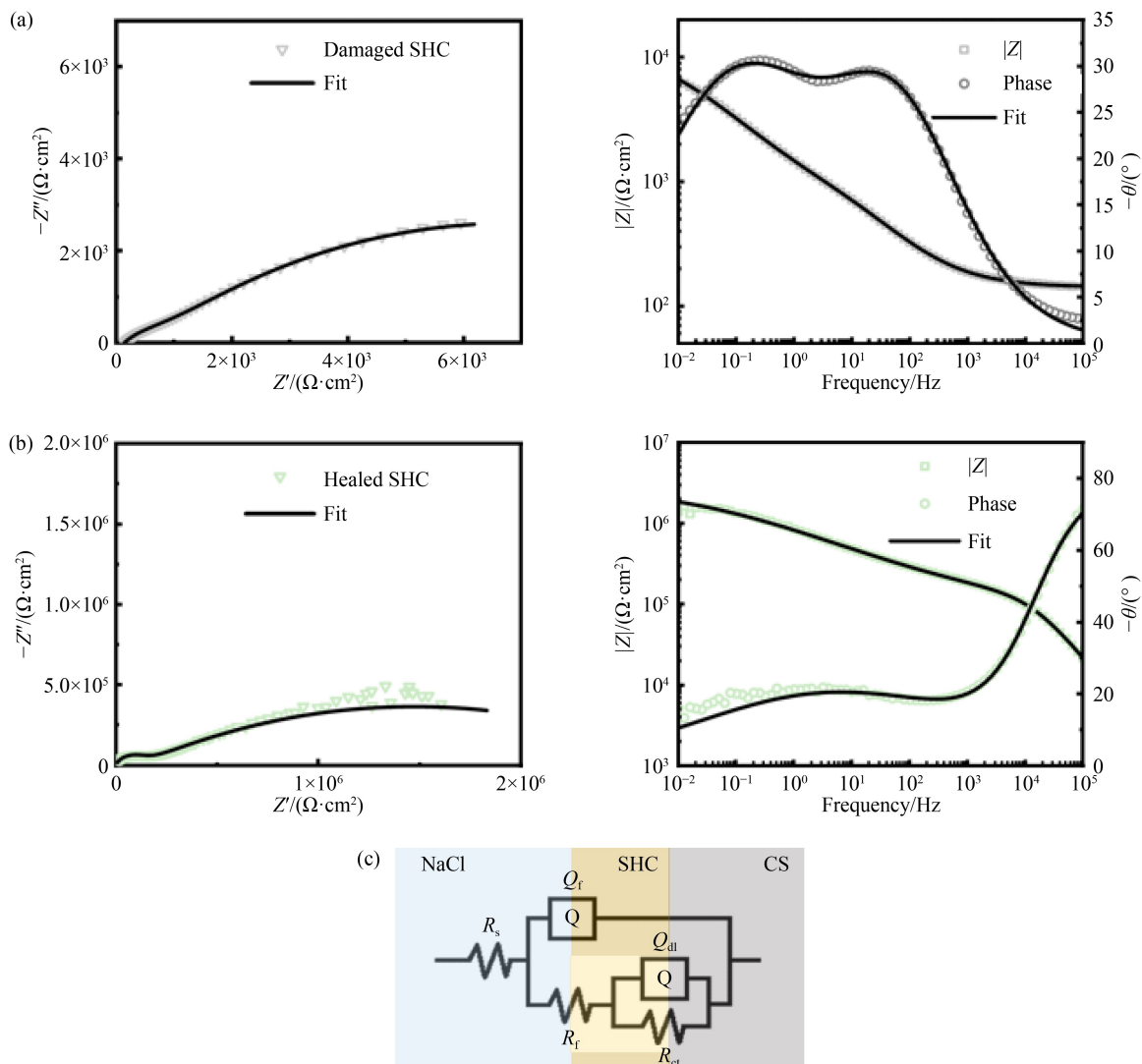


**Fig. 8** EIS plots of the damaged SHC before (a) and after (b) the self-healing process; (c) equivalent circuit of both the damaged and healed SHC.



penetrate throughout the defect due to the filling of tetradecanol. The  $Q_f$  of the healed SHC can reach ca.  $10^{-10} \text{ F}\cdot\text{cm}^{-2}\cdot\text{s}^{n-1}$  (Table 2), which is close to the intact value (ca.  $10^{-11} \text{ F}\cdot\text{cm}^{-2}\cdot\text{s}^{n-1}$ ), reflecting the decreased coating permeability. As expected, the value of  $Q_{dl}$  also decreases from ca.  $10^{-4}$  to ca.  $10^{-7} \text{ F}\cdot\text{cm}^{-2}\cdot\text{s}^{n-1}$ , indicating that corrosion active sites are significantly reduced. The corrosion protection efficiency of the healed coating can reach 99.77%, which is only a small decrease compared to the intact coating.

### 3.6 Stability of the SHC in 3.5 wt% NaCl aqueous solution

To explore the stability of the SHC, we investigated the corrosive behavior of the SHC-coated CS after 168 h of immersion in a 3.5 wt% NaCl solution as shown in Fig. 10. Figures 10(a) and 10(b) present the Bode-modulus and Bode-phase plots of the SHC-coated CS in 3.5 wt% NaCl solution for 168 h. In Fig. 10(a), it seems that  $|Z|_{0.01\text{Hz}}$  slightly decreases with time due to the gradual penetration electrolyte, but it remains the same order of magnitude. During the entire immersion process, only one broad peak is detected in Fig. 10(b), indicating that penetration of the corrosive medium is insufficient to change the corrosion process model. Therefore, R(QR)(QR) is used for the equivalent circuit of the SHC-coated CS. After immersion in 3.5 wt% NaCl for 48 h, the  $R_{ct}$  of the SHC-coated CS remained at  $1.15 \times 10^6 \Omega\cdot\text{cm}^2$  (Fig. 10(d)), revealing that the coating could still impede the current flow from anodic to cathodic areas. As the immersion time increases, over 168 h, the  $R_{ct}$  of the coating can still remain the same order of magnitude with a value of  $2.63 \times 10^6 \Omega\cdot\text{cm}^2$ , so the decrease in the impedance modulus at low frequencies is nearly negligible. In fact, the  $R_{ct}$  of the SHC-coated CS is nearly unchanged throughout the immersion process. In addition, the  $Q_f$  values of the healed SHC only show a small fluctuation ( $> 10^{-7} \text{ F}\cdot\text{cm}^{-2}\cdot\text{s}^{n-1}$ ) (Table 3),

reflecting the low variation in coating permeability.  $Q_{dl}$  values are in the range from ca.  $10^{-7}$  to ca.  $10^{-11} \text{ F}\cdot\text{cm}^{-2}\cdot\text{s}^{n-1}$ , lower than bare CS (ca.  $10^{-4} \text{ F}\cdot\text{cm}^{-2}\cdot\text{s}^{n-1}$ ), indicating less occurrence of corrosion reactions during immersion. This demonstrates the excellent performance of the SHC in the corrosion protection of CS.

## 4 Conclusions

In this work, we successfully achieved an anti-corrosion coating with sunlight-assisted self-healing ability by integrating photothermal particles and a phase change material with epoxy resin via an extremely simple method.  $\text{Fe}_3\text{O}_4$  nanoparticles were used as photothermal materials with a narrow bandgap. High-energy solar irradiation enables the formation of above-bandgap electron-hole pairs. With the relaxation of these above-bandgap electron-hole pairs to the band edges, extra energy is converted into heat, which is spontaneously transferred from high-temperature  $\text{Fe}_3\text{O}_4$  nanoparticles to adjacent tetradecanol by heat conduction, melting the tetradecanol. Therefore, this coating shows good photothermal performance, allowing the transition of tetradecanol into liquid, which flows and fills coating defects under solar irradiation. Due to this self-healing effect, the obtained coating can handle defects, including perforations and scratches. In addition, similar to the pure commercial coating, this coating can provide a pronounced physical barrier to resist the penetration of corrosive media, demonstrating good anti-corrosion performance. The healed SHC coating can still serve as a good barrier for the underlying CS. All materials for SHC fabrication are commercially available, and the entire preparation process is very facile. It is envisioned that these benefits will allow for the mass production of such a type of SHC for corrosion protection of outdoor facilities.

**Table 2** Electrochemical parameters of the intact, damaged and healed SHCs

Material	$R_f/(\Omega\cdot\text{cm}^2)$	$Q_f-Y_0/(\text{F}\cdot\text{cm}^{-2}\cdot\text{s}^{n-1})$	$Q_f-n$	$R_{ct}/(\Omega\cdot\text{cm}^2)$	$Q_{dl}-Y_0/(\text{F}\cdot\text{cm}^{-2}\cdot\text{s}^{n-1})$	$Q_{dl}-n$
Intact SHC	$7.02 \times 10^6$	$3.28 \times 10^{-11}$	0.98	$3.84 \times 10^6$	$4.70 \times 10^{-11}$	0.89
Damaged SHC	$1.20 \times 10^3$	$1.08 \times 10^{-4}$	0.56	$1.16 \times 10^4$	$3.28 \times 10^{-4}$	0.50
Healed SHC	$1.15 \times 10^5$	$3.19 \times 10^{-10}$	0.89	$2.71 \times 10^6$	$5.65 \times 10^{-7}$	0.34

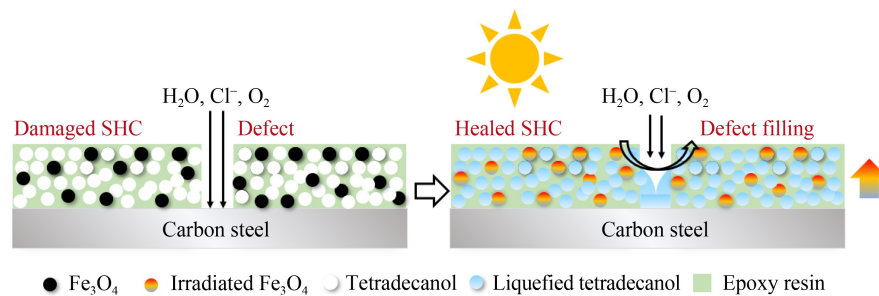


**Fig. 9** Corrosion protection mechanism of the intact, damaged and healed SHCs.

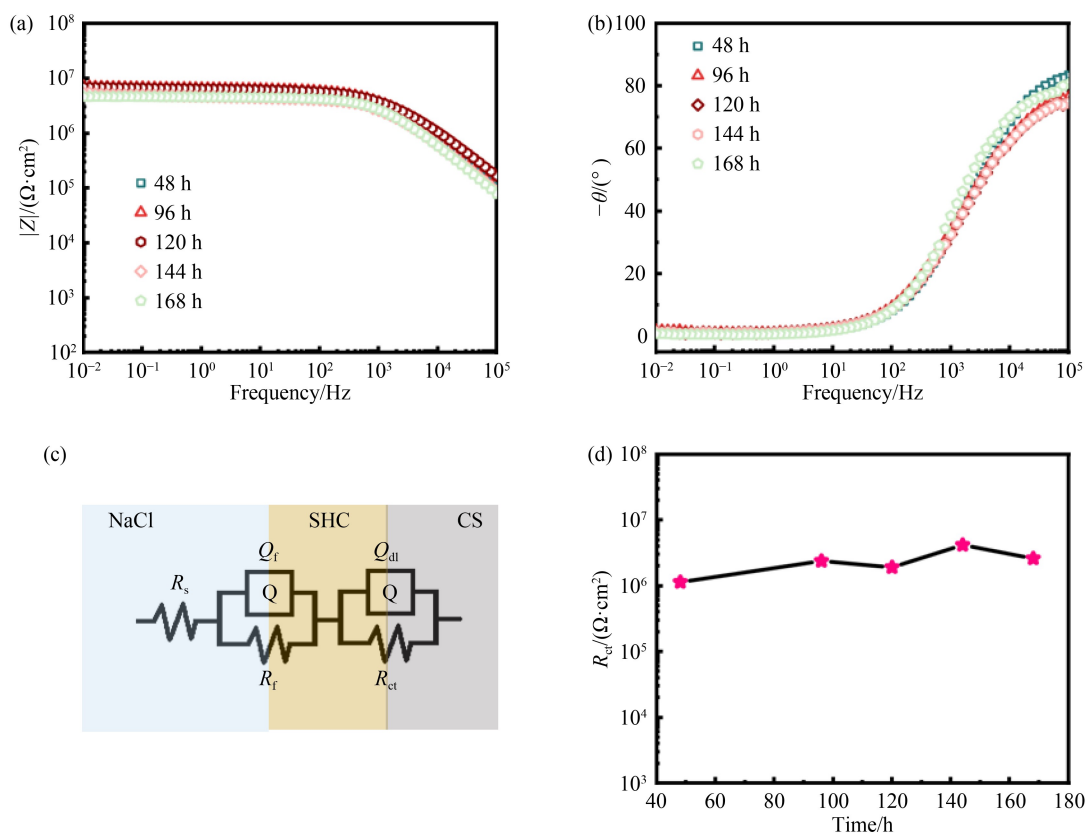


**Fig. 10** (a) Bode-modulus and (b) Bode-phase plots of the SHC with time; (c) equivalent circuit of the SHC; (d)  $R_{ct}$  evolution of the SHC coating with time.

**Table 3** Electro parameters of the fitting results of the SHC-coated CS with time

Time/h	$R_f/(\Omega \cdot \text{cm}^2)$	$Q_f - Y_0/(\text{F} \cdot \text{cm}^{-2} \cdot \text{s}^{n-1})$	$Q_f - n$	$R_{ct}/(\Omega \cdot \text{cm}^2)$	$Q_{dl} - Y_0/(\text{F} \cdot \text{cm}^{-2} \cdot \text{s}^{n-1})$	$Q_{dl} - n$
48	$4.83 \times 10^6$	$7.83 \times 10^{-11}$	0.87	$1.15 \times 10^6$	$3.75 \times 10^{-7}$	0.53
96	$4.31 \times 10^6$	$5.38 \times 10^{-10}$	0.77	$2.41 \times 10^6$	$7.58 \times 10^{-11}$	0.89
120	$4.73 \times 10^6$	$1.00 \times 10^{-10}$	0.83	$1.93 \times 10^6$	$4.82 \times 10^{-9}$	0.70
144	$1.22 \times 10^6$	$5.58 \times 10^{-7}$	0.48	$4.22 \times 10^6$	$1.39 \times 10^{-10}$	0.85
168	$1.97 \times 10^6$	$7.76 \times 10^{-10}$	0.83	$2.63 \times 10^6$	$1.07 \times 10^{-10}$	0.89

**Acknowledgments** This research was funded by the National Natural Science Fund for Distinguished Young Scholars (Grant No. 51525903), the National Natural Science Foundation of China (Grant Nos. 51989292 and 51909291) and the International Science and Technology Cooperation Program of Guangdong Province (Grant No. 2019A050510020).

**Electronic Supplementary Material** Supplementary material is available in the online version of this article at <https://dx.doi.org/10.1007/s11705-022-2147-1> and is accessible for authorized users.

## References

- Akhondi M, Jamalizadeh E. Fabrication of beta-cyclodextrin modified halloysite nanocapsules for controlled release of corrosion inhibitors in self-healing epoxy coatings. *Progress in Organic Coatings*, 2020, 145: 105676
- Amini M, Naderi R, Mandavian M, Badii A. Effect of piperazine functionalization of mesoporous silica type SBA-15 on the loading efficiency of 2-mercaptobenzothiazole corrosion inhibitor. *Industrial & Engineering Chemistry Research*, 2020, 59(8): 3394–3404
- Arakalam I O, Madu I O, Ishidi E Y. High performance characteristics of *Lupinus arboreus* gum extract as self-healing and corrosion inhibition agent in epoxy-based coating. *Progress in Organic Coatings*, 2021, 151: 106095
- Dehghani A, Bahlakeh G, Ramezanzadeh B. Construction of a sustainable/controlled-release nano-container of non-toxic corrosion inhibitors for the water-based siliconized film: estimating the host-guest interactions/desorption of inclusion complexes of cerium acetylacetonate (CeA) with beta-cyclodextrin (beta-CD) via detailed electronic/atomic-scale computer modeling and experimental methods. *Journal of Hazardous Materials*, 2020, 399: 123046
- Dehghani A, Bahlakeh G, Ramezanzadeh B. Beta-cyclodextrin-

- zinc acetylacetonate (beta-CD@ZnA) inclusion complex formation as a sustainable/smart nanocarrier of corrosion inhibitors for a water-based siliconized composite film: integrated experimental analysis and fundamental computational electronic/atomic-scale simulation. *Composites Part B: Engineering*, 2020, 197: 108152
6. Kim C, Karayan A I, Milla J, Hassan M, Castaneda H. Smart coating embedded with pH-responsive nanocapsules containing a corrosion inhibiting agent. *ACS Applied Materials & Interfaces*, 2020, 12(5): 6451–6459
  7. Tan Z Y, Wang S, Hu Z R, Chen W L, Qu Z C, Xu C G, Zhang Q, Wu K, Shi J, Lu M G. pH-responsive self-healing anticorrosion coating based on a lignin microsphere encapsulating inhibitor. *Industrial & Engineering Chemistry Research*, 2020, 59(7): 2657–2666
  8. Wang Q, Wang W, Ji X H, Hao X P, Ma C C, Hao W, Li X L M, Chen S G. Self-healing coatings containing core-shell nanofibers with pH-responsive performance. *ACS Applied Materials & Interfaces*, 2021, 13(2): 3139–3152
  9. Lei Y H, Qiu Z C, Tan N, Du H L, Li D D, Liu J R, Liu T, Zhang W G, Chang X T. Polyaniline/CeO<sub>2</sub> nanocomposites as corrosion inhibitors for improving the corrosive performance of epoxy coating on carbon steel in 3.5% NaCl solution. *Progress in Organic Coatings*, 2020, 139: 105430
  10. Bao Y, Yan Y, Wei Y M, Ma J Z, Zhang W B, Liu C. Salt-responsive ZnO microcapsules loaded with nitrogen-doped carbon dots for enhancement of corrosion durability. *Journal of Materials Science*, 2021, 56(8): 5143–5160
  11. Feng Y Y, Cui Y X, Zhang M J, Li M L, Li H Y. Preparation of tung oil-loaded PU/PANI microcapsules and synergetic anti-corrosion properties of self-healing epoxy coatings. *Macromolecular Materials and Engineering*, 2021, 306(2): 2000581
  12. Malekhouyan R, Khorasani S N, Neisiany R E, Torkaman R, Koochaki M S, Das O. Preparation and characterization of electrosprayed nanocapsules containing coconut-oil-based alkyd resin for the fabrication of self-healing epoxy coatings. *Applied Sciences*, 2020, 10(9): 3171
  13. Neto A G C, Pellanda A C, Jorge A R D, Floriano J B, Berton M A C. Preparation and evaluation of corrosion resistance of a self-healing alkyd coating based on microcapsules containing tung oil. *Progress in Organic Coatings*, 2020, 147: 105874
  14. Chen G M, Sun Z Y, Wang Y M, Zheng J Y, Wen S F, Zhang J W, Wang L, Hou J, Lin C G, Yue Z F. Designed preparation of silicone protective materials with controlled self-healing and toughness properties. *Progress in Organic Coatings*, 2020, 140: 105483
  15. Dolatkhan A, Wilson L D. Saline-responsive and hydrogen bond gating effects in self-healing polyaniline. *ACS Applied Polymer Materials*, 2020, 2(6): 2311–2318
  16. Nardeli J V, Fugivara C S, Taryba M, Montemor M F, Benedetti A V. Self-healing ability based on hydrogen bonds in organic coatings for corrosion protection of AA1200. *Corrosion Science*, 2020, 177: 108984
  17. Bai Z G, Bai Y Y, Zhang G P, Wang S Q, Zhang B. A hydrogen bond based self-healing superhydrophobic octadecyltriethoxysilane-lignocellulose/silica coating. *Progress in Organic Coatings*, 2021, 151: 106104
  18. Chen T Q, Fang L, Li X, Gao D S, Lu C H, Xu Z Z. Self-healing polymer coatings of polyurea-urethane/epoxy blends with reversible and dynamic bonds. *Progress in Organic Coatings*, 2020, 147: 105876
  19. Dong Y H, Geng C D, Liu C M, Gao J, Zhou Q. Near-infrared light photothermally induced shape memory and self-healing effects of epoxy resin coating with polyaniline nanofibers. *Synthetic Metals*, 2020, 266: 116417
  20. Nicolas-Boluda A, Yang Z, Guilbert T, Fouassier L, Carn F, Gazeau F, Pileni M P. Self-assemblies of Fe<sub>3</sub>O<sub>4</sub> nanocrystals: toward nanoscale precision of photothermal effects in the tumor microenvironment. *Advanced Functional Materials*, 2021, 31(4): 2006824
  21. Chen R, Wu Z, Zhang T, Yu T, Ye M. Magnetically recyclable self-assembled thin films for highly efficient water evaporation by interfacial solar heating. *RSC Advances*, 2017, 7(32): 19849–19855
  22. Ekariyani N Y, Wardani D P, Suharyadi E, Daryono B S, Abraha K. The use of Fe<sub>3</sub>O<sub>4</sub> magnetic nanoparticles as the active layer to detect plant's DNA with surface plasmon resonance (SPR) based biosensor. *AIP Conference Proceedings*, 2016, 1755(1): 150016
  23. Zuo J G, Li W Z, Weng L D. Thermal properties of lauric acid/1-tetradecanol binary system for energy storage. *Applied Thermal Engineering*, 2011, 31(6-7): 1352–1355
  24. Tian T, Song J, Niu L B, Feng R X. Preparation and properties of 1-tetradecanol/1,3:2,4-di-(3,4-dimethyl) benzylidene sorbitol gelatinous form-stable phase change materials. *Thermochimica Acta*, 2013, 554: 54–58
  25. Cheng F, Zhang X, Wen R, Huang Z, Fang M, Liu Y, Wu X, Min X. Thermal conductivity enhancement of form-stable tetradecanol/expanded perlite composite phase change materials by adding Cu powder and carbon fiber for thermal energy storage. *Applied Thermal Engineering*, 2019, 156: 653–659
  26. Zeng J L, Gan J, Zhu F R, Yu S B, Xiao Z L, Yan W P, Zhu L, Liu Z Q, Sun L X, Cao Z. Tetradecanol/expanded graphite composite form-stable phase change material for thermal energy storage. *Solar Energy Materials and Solar Cells*, 2014, 127: 122–128
  27. Mu B Y, Li M. Fabrication and thermal properties of tetradecanol/graphene aerogel form-stable composite phase change materials. *Scientific Reports*, 2018, 8(1): 14
  28. Chen C, Kuang Y, Hu L. Challenges and opportunities for solar evaporation. *Joule*, 2019, 3(3): 683–718
  29. Duncan A B, Peterson G P. Review of microscale heat transfer. *Applied Mechanics Reviews*, 1994, 47(9): 397–428
  30. Daroonparvar M, Khan M U F, Saadeh Y, Kay C M, Kasar A K, Kumar P, Esteves L, Misra M, Menezes P, Kalvala P R, et al. Modification of surface hardness, wear resistance and corrosion resistance of cold spray Al coated AZ31B Mg alloy using cold spray double layered Ta/Ti coating in 3.5 wt% NaCl solution. *Corrosion Science*, 2020, 176: 109029
  31. Hao Z, Chen C, Shen T, Lu J, Yang H C, Li W. Slippery liquid-infused porous surface via thermally induced phase separation for enhanced corrosion protection. *Journal of Polymer Science*, 2020, 58(21): 3031–3041
  32. Xiong L, Liu J, Yu M, Li S. Improving the corrosion protection

- properties of PVB coating by using salicylaldehyde@ZIF-8/graphene oxide two-dimensional nanocomposites. *Corrosion Science*, 2019, 146: 70–79
33. Brug G J, van den Eeden A L G, Sluyters-Rehbach M, Sluyters J H. The analysis of electrode impedances complicated by the presence of a constant phase element. *Journal of Electroanalytical Chemistry and Interfacial Electrochemistry*, 1984, 176(1): 275–295
34. Hsu C H, Mansfeld F. Concerning the conversion of the constant phase element parameter  $Y_0$  into a capacitance. *Corrosion*, 2001, 57(9): 747–748